Separation and Purification Technology 336 (2024) 126219

Contents lists available at ScienceDirect

Separation and Purification Technology

journal homepage: www.elsevier.com/locate/seppur

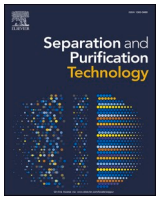

Influence of SO_2 on CO_2 capture by adsorption on activated carbon: Individual pore performance via multiscale simulation

Davi D.S. Moreira [a], Daniel V. Gonçalves [a], Juliana A. Coelho [a], Diana C.S. de Azevedo [a], Rafael B. Rios [b], Sebastião M.P. de Lucena [a], Moises Bastos-Neto [a,*]

[a] Grupo de Pesquisa em Separações por Adsorção (GPSA), Department of Chemical Engineering, Campus do Pici, bl. 731, Federal University of Ceará, Fortaleza, CE 60760-400, Brazil

[b] Department of Engineering and Technology, Federal University of the Semi-Arid Region (UFERSA), Mossoró, RN 59625-900, Brazil

ARTICLE INFO

Editor: S. Yi

Keywords:
CO_2
SO_2
Adsorption
Activated carbon
Column dynamics
Flue gas

ABSTRACT

Carbon capture under post-combustion conditions has been the topic of numerous studies in the last decade. Although exhaust gases typically contain different components other than CO_2, they are commonly neglected in these studies. The presence of sulfur dioxide, for example, tends to interfere in the carbon capture process through different mechanisms. The present work aimed to evaluate the effects of SO_2 on the CO_2 retention capacity through the integration of experimental evaluation, column dynamics modeling and molecular simulation (multiscale modeling) for an activated carbon sample under typical conditions found in the post-combustion environment. Results indicate that, under typical post-combustion flue gas conditions, SO_2 has little influence on the CO_2 retention capacity of the carbon in comparison to other adsorbent materials. The highest concentration of SO_2 (5 000 ppmv) led to a decrease of approximately 10 % in the CO_2 capture capacity. Significant deactivation (around 40 %) was observed experimentally and by molecular simulation only for very high concentrations of SO_2 (50 000 ppmv). Additionally, no evidence of reactions with the material was found and both captured components could be completely desorbed by means of suitable regeneration methods. To access individual pore performance, molecular simulations were implemented for SO_2 adsorption using, for the first time, a rigorous heterogeneous pore model (rMD). The results revealed a large deactivation for the 7.0 Å pore, a surprising cooperative effect for the 8.9 Å pore, and indifference for the larger 18.5 and 27.9 Å pores. For SO_2 concentrations up to 5 000 ppmv, the use of carbon-based adsorbent could rule out the need of a pre-treatment operation to remove SO_2 in carbon capture processes. For higher concentrations, molecular simulation showed that tailoring carbon porosity in the range of 7 Å to 8.9 Å considerably reduces the interference of SO_2. Results also point out that the IAST and Langmuir models diverge from the molecular simulation results, particularly at low loadings (up to 5 000 ppmv SO_2), indicating the need for caution when applying these models in systems where competitive interactions between molecules are relevant, as is the case with mixtures of CO_2 and SO_2.

1. Introduction

Worldwide industrial activity and power sources are still based on combustion processes to a great extent [1,2]. As a consequence of the growing energy demand and industrial development, a continuous increase in emissions of atmospheric pollutants such as CO_2 has been observed. From an environmental perspective, CO_2 is claimed as one of the main causes of the intensification of the greenhouse effect, which in turn closely relates to global warming and climate change. Therefore, several policies and agreements have been set with the purpose of emission control [3,4]. According to the International Energy Agency (IEA), around 32 billion tons of CO_2 were emitted worldwide in 2020, nearly 90 % coming from energy production [5,6].

Several strategies have been proposed to reduce CO_2 emissions to acceptable levels. The most widespread technologies used to separate and capture CO_2 are chemical absorption, membrane separation, cryogenic distillation, and adsorption [7–9]. In this context, adsorption-based CO_2 capture has been gaining attention due to its relatively lower operating costs and good efficiency as compared to other technologies [10,11].

* Corresponding author.
E-mail address: mbn@ufc.br (M. Bastos-Neto).

https://doi.org/10.1016/j.seppur.2023.126219
Received 8 November 2023; Received in revised form 18 December 2023; Accepted 26 December 2023
Available online 2 January 2024

In addition to carbon dioxide, combustion gases contain other harmful components. The typical composition (v/v) of flue gases is 72 – 74 % N_2, 4.8 – 26.9 % CO_2, 9 – 13.8 % H_2O, 0.7 – 15 % O_2, and trace compounds, such as particulate matter, sulfur, and nitrogen oxides [12]. These components tend to interfere with the efficiency of CO_2 capture processes by different mechanisms, such as the deactivation of the adsorbent and competition for adsorption sites [13–15].

Despite the low concentration, often ranging from 500 to 5 000 ppmv, sulfur dioxide can affect CO_2 capture by adsorption not only by competing for the adsorption sites but also by undergoing parallel chemical reactions that inactivate CO_2 adsorption sites [2,15–19].

Literature dealing with the impacts of the presence of SO_2 in CO_2 capture processes is still scarce and there is no definitive consensus on the configuration of separation units to take into account the presence of this contaminant [20]. Some studies suggest the use of pretreatment sections in order to dry and purify the flue gas (*i.e.*, to remove SO_2, NO_x and H_2O) before capturing CO_2 [17,21,22], while other authors propose a single separation unit in which both components (SO_2 and CO_2) can be removed simultaneously, provided that a suitable adsorbent is used [23–25].

The choice of a suitable and robust adsorbent is therefore crucial to maximize the efficiency of CO_2 capture. Literature reports high SO_2/CO_2 selectivities on different adsorbents such as MOFs [26–28], mesoporous silicas [19,29,30], zeolites [15,31,32] and activated carbons [11,33–35]. Although materials with preferential adsorption for CO_2 over SO_2 are currently unknown, activated carbons can show lower SO_2/CO_2 selectivity, which makes them promising materials for CO_2 capture in the presence of SO_2 traces.

Most industrial separation and purification systems based on selective adsorption use packed columns that operate under adsorption–desorption cycles. Thus, the evaluation of the dynamic behavior of SO_2/CO_2 in an adsorbent bed can provide a more realistic understanding of this type of process [36–38]. Furthermore, the generated experimental data can be used to validate mathematical models capable of accurately describing the separation dynamics and performance, which is an essential part of the study. As a matter of fact, process simulation has been increasingly used as a tool for this purpose, since it reduces costs related to experiments on lab or pilot scales [39,40].

Given the limited availability of studies investigating the impact of SO_2 on CO_2 capture processes, particularly under conditions found in post-combustion scenarios, molecular simulation methods were employed to allow for a deeper understanding of the underlying mechanisms of SO_2 and CO_2 competitive adsorption in individual pores of the activated carbon. To the best of our knowledge, no method based on molecular simulation to predict the adsorption of SO_2 in carbonaceous materials has been reported. In this study, a novel heterogeneous model to represent activated carbon is proposed, considerably improving the prediction of isotherms.

Experimental breakthrough curves were obtained for single component SO_2 and CO_2, as well as a for typical SO_2/CO_2 mixture. A mathematical model was subsequently proposed to describe the dynamic adsorption of these mixtures in a fixed bed and its validity was confirmed by experimental data. In parallel, molecular simulations were performed to predict adsorption within four representative carbon pores for the SO_2/CO_2 mixture. These simulation results were then cross-referenced with column dynamics simulations for SO_2 in mixtures with CO_2. This cross-referencing aimed to confirm the reliability of the process simulations. Furthermore, the study included a comparison of values for carbon deactivation induced by SO_2. These values were obtained from column dynamics simulations (mathematical model) based on the IAST and Langmuir models, and they were compared with results derived from molecular simulations. Emphasis is placed on the fact that the results achieved in this study were made possible solely through a multiscale approach to the problem. The contribution and correlations between the employed techniques, such as the experimental procedure, macroscopic modeling of the column, and fundamentals at the atomic level (molecular simulation), are detailed in Fig. 1.

2. Material and methods

2.1. Materials

A granular activated carbon of 18 × 30 mesh (1.0 to 0.595 mm) supplied by Indústrias Químicas Carbomafra S.A. (Brazil), namely C141-S, was used in this study. The experiments were performed using helium (99.99 %), carbon dioxide (99.8 %) and sulfur dioxide (99.9 %). Nitrogen (99.99 %) was used to determine the textural properties of the adsorbent. All gases were supplied by White Martins Praxair Inc. (Brazil).

2.2. Textural characterization

The activated carbon sample was characterized by adsorption–desorption isotherms of N_2 at 77 K obtained with an Autosorb-iQ3 (Quantachrome Instruments, USA). From the N_2 isotherms, the textural properties were determined: specific surface area using the method proposed by Brunauer-Emmett-Teller (BET); total pore volume through the adsorbed volume at $P/P_0 \approx 1$ (assuming that the pores are totally filled with liquid adsorbate); and the micropore volume using the Dubinin-Radushkevich (DR) model [41].

2.3. Single component isotherms

The adsorption isotherms of pure CO_2 and SO_2 were obtained by gravimetry with the aid of a magnetic suspension balance (Rubotherm, Germany) equipped with a gas dosing system. The isotherms were measured at 303, 323 and 343 K and pressures ranging from vacuum (0.001 bar) to 2.0 bar. Prior to the equilibrium measurements, the activated carbon sample was degassed under vacuum (0.001 bar) at a temperature of 423 K for 12 h (with a heating ramp of 3 K min^{-1}) until no mass loss was detected. Experiments with helium were carried out to determine the volume of the solid phase and to assess the buoyancy effects. More details about the applied experimental procedure can be found in the literature [42–48].

The Langmuir equilibrium model was fitted to the isotherms of pure components. The model parameters were obtained by simultaneously fitting the Langmuir equation to the isotherms obtained at the three temperatures (303, 323 and 343 K). The isosteric heat of adsorption for each component (ΔH_i^{iso}) was also estimated from isotherm data using the Clausius-Clapeyron equation (Equation (01) according to the methodology described by Rouquerol *et al.* [41].

$$\Delta H_i^{iso} = R\left(\frac{\partial}{\partial\left(1/T_g\right)}\ln(P)\right)_q \tag{01}$$

where R is the ideal gas constant, T_g is the gas temperature, P is the pressure and the derivative has to be evaluated at a constant surface loading (q).

2.4. Column dynamics

Single and multicomponent fixed bed adsorption experiments were carried out in a fixed bed unit assembled and used in previous studies [49–51]. The system consists of mass flow controllers, pressure regulating valves, a pressure transducer, a multi-loop valve, a data acquisition system and two GCs connected in series.

In this study, breakthrough curves were measured for different gas feeds, as shown in Table 1. All experiments were performed at pressures (P_{total}) of approximately 1.3 bar, temperatures of 323 and/or 343 K, and a total volumetric flow of 100 mL min^{-1}. The adsorbent was packed in a stainless-steel column 0.25 m long and 0.005 m of internal diameter.

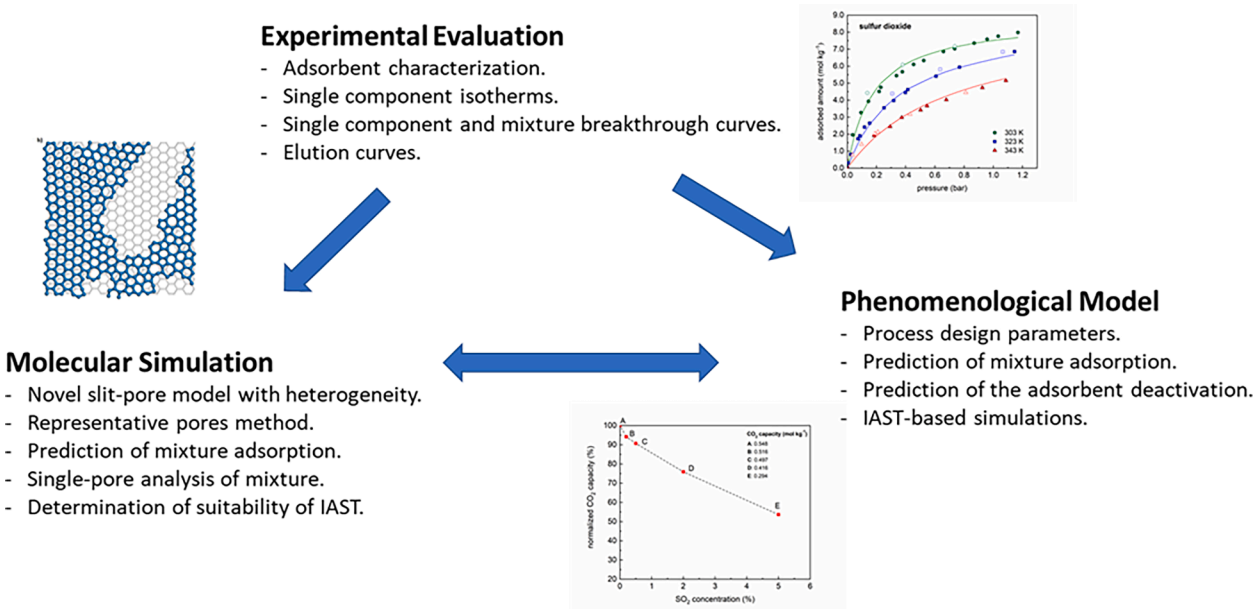

Fig. 1. Schematic illustration of the contributions associated with each area of the multiscale modeling approach.

Table 1
Feed composition of the column dynamics experiments.

feed (diluted in He)	composition	volumetric flow (mL min^{-1})		
		CO_2	SO_2	He
CO_2	12 % CO_2	12	–	88
SO_2	5 % SO_2	–	5	95
$CO_2 + SO_2$	12 % CO_2 + 5 % SO_2	12	5	83

After being packed, the adsorbent underwent a regeneration process using a flow of helium (inert) of 15 mL min^{-1} for 12 h at 423 K. At the end of the regeneration procedure, the column temperature was set to the desired experimental condition. After adjusting the flow rates of each component, the gas mixture was fed to the bed and gas aliquots were captured at the bed outlet at predefined times until its complete saturation. At this point, the flow was stopped and the gas samples were analyzed to determine the relationship between the outlet and the inlet concentrations. All experimental runs were carried out in duplicates in order to ensure repeatability. The amount adsorbed of each component was estimated using the procedure described by Wilkins *et al.* [52].

The feed rate of each component in the column was set to obtain a gas mixture of composition as close as possible to that of typical flue gases. Due to system limitations in terms of detection sensitivity and flow control, a concentration of 5 % (5 000 ppmv) SO_2, which is higher than typical values found in exhaust gases, was used. In spite of that, the proposed experimental conditions provide some insights and a good understanding of the equilibrium and kinetics of the components in the adsorbent material. Additionally, the results were used to validate a dynamic model, which, in principle, allows the evaluation of different conditions of pressure, temperature and concentration.

2.5. Mathematical model

The mathematical model implemented in this study consists of mass, energy and momentum balances describing the phenomena taking place simultaneously during the adsorption-based separation process. Given the complexity of the system, mainly with regard to the mechanisms of mass transfer between the phases and the gas–solid adsorption equilibrium, some assumptions were made to simplify the process modeling. The main ones are: (i) ideal gas behavior of the gas phase throughout the bed; (ii) plugged flow with constant axial mass dispersion along the flow; (iii) mass transfer rate described by the linear driving force (LDF) model; (iv) non-isothermal and non-adiabatic conditions; (v) mass, heat and velocity gradients in the radial direction are negligible [40,52–56].

The mass balance of each component in the fluid phase is written in the form of Equation (02) [49,56,57].

$$\frac{\partial}{\partial z}\left(\varepsilon D_{ax} C_{g,T}\frac{\partial y_i}{\partial z}\right) - \frac{\partial}{\partial z}\left(uC_{g,i}\right) - \varepsilon\frac{\partial C_{g,i}}{\partial t} - (1-\varepsilon)\left(\varepsilon_p\frac{\partial C_{g,i}}{\partial t} + \rho_p\frac{\partial \bar{q}_i}{\partial t}\right) = 0 \tag{02}$$

where $C_{g,T}$ and $C_{g,i}$ are the total and component i gas phase concentrations, respectively; D_{ax} is the axial dispersion coefficient of the gas mixture; y_i represents the molar fraction of component i; u is the superficial velocity; ε is the bed porosity; ε_p is the particle porosity; ρ_p is the particle density; and $\bar{q}_i$ is the average adsorbed concentration of component i.

The mass transfer rate of each component in the adsorbent is given by Equation (03):

$$\frac{\partial \bar{q}_i}{\partial t} = k_{LDF}\left(q_i^* - \bar{q}_i\right) \tag{03}$$

where k_{LDF} is the lumped mass transfer coefficient, and q_i^* is the amount adsorbed of the component i at equilibrium. In this work, the Extended Langmuir model (Equation (04) was used to describe the adsorption equilibrium.

$$q_i^* = \frac{q_{max,i} b_i P_i}{1 + \sum_{j=1}^{n} b_j P_j} \tag{04}$$

It was assumed that the adsorbent particle approaches a spherical shape and that the controlling step for the diffusion of species occurs in the micropore size range. As a consequence, the LDF constant, k_{LDF}, may be written according Equation (05) [47].

$$k_{LDF} = 15\frac{D_{\mu,i}}{r_\mu^2} \tag{05}$$

where $D_{\mu,i}$ is the micropore diffusivity of component i; and r_μ is the micropore radius of the adsorbent. The values of D_μ/r_μ^2 were estimated by the best fit of the mathematical model to the experimental data [47].

The homogeneous energy balance that relates both phases (solid and gas) was expressed by Equation (06) [49,58–60].

$$\frac{\partial}{\partial z}\left(\lambda\frac{\partial T_g}{\partial z}\right) - uC_{g,T}\widetilde{c}_{p,g}\frac{\partial T_g}{\partial z} + \varepsilon RT_g\frac{\partial C_{g,T}}{\partial t} - 4\frac{h_w}{d_i}\left(T_g - T_w\right)$$

$$-\left[\varepsilon C_{g,T}\widetilde{c}_{v,g} + (1-\varepsilon)\left(\varepsilon_p\sum_{i=1}^{n}C_{g,i}\widetilde{c}_{v,g,i} + \rho_p\sum_{i=1}^{n}\bar{q}_i\widetilde{c}_{v,ads,i} + \rho_p\widehat{c}_{p,s}\right)\right]\frac{\partial T_g}{\partial t}$$

$$+(1-\varepsilon)\varepsilon_p RT_g\frac{\partial C_{g,T}}{\partial t} + \rho_b\sum_{i=1}^{n}\left(-\Delta H_i^{iso}\right)\frac{\partial\bar{q}_i}{\partial t} = 0 \quad (06)$$

where λ is the axial heat dispersion coefficient; T_g and T_w are the gas and the column wall temperatures, respectively; h_w is the film heat transfer coefficient between the gas and the column wall; $\widetilde{c}_{p,g}$ and $\widetilde{c}_{v,g}$ are the gas mixture molar specific heat at constant pressure and constant volume, respectively; $\widetilde{c}_{v,g,i}$ is the molar specific heat of component i at constant volume; $\widetilde{c}_{v,\,ads,i}$ is the molar specific heat of component i in the adsorbed phase at constant volume; $\widehat{c}_{p,s}$ is the specific heat of the particle at constant pressure (per mass unit); d_i is the column internal diameter; ρ_b is the bed density; and ΔH_i^{iso} is the heat of adsorption of component i.

The energy balance for the column wall was expressed by Equations (07) to (09) [39,49,60].

$$\rho_w\widehat{c}_{p,w}\frac{\partial T_w}{\partial t} = \alpha_w h_w\left(T_g - T_w\right) - \alpha_{wL}U\left(T_w - T_\infty\right) \quad (07)$$

$$\alpha_w = \frac{d_i}{e(d_i + e)} \quad (08)$$

$$\alpha_{wL} = \frac{2}{(d_i + e)\ln\left(\frac{d_i+2e}{d_i}\right)} \quad (09)$$

where ρ_w is the wall density; $\widehat{c}_{p,w}$ is the specific heat of the wall at constant pressure; α_w is the ratio of the internal surface area of the column to the volume of the column wall; α_{wL} is the ratio of the logarithmic mean surface area of the column to the volume of the column wall; U is the overall heat transfer coefficient; e is the wall thickness; and T_∞ is the ambient temperature.

The Ergun equation (Equation (10) was used to describe the pressure drop in the packed bed [49,57,58,60–62].

$$-\frac{\partial P}{\partial z} = \frac{150\mu(1-\varepsilon)^2}{\varepsilon^3 {d_p}^2}u + \frac{1,75(1-\varepsilon)\rho_g}{\varepsilon^3 d_p}|u|u \quad (10)$$

where μ is the viscosity of the gas mixture; d_p is the particle diameter; and ρ_g is the density of the gas mixture.

The following series of boundary and initial conditions (Equations (11) to (17) were necessary to solve the system of coupled partial equations.

$$z = 0 u^{inlet}C_{g,i}{}^{inlet} = u|_{z=0}C_{g,i}\big|_{z=0} - \varepsilon D_{ax}C_{g,T}\big|_{z=0}\frac{\partial y_i}{\partial z}\Big|_{z=0} \quad (11)$$

$$z = L\frac{\partial C_{g,i}}{\partial z}\Big|_{z=L} = 0 \quad (12)$$

$$z = 0 u^{inlet}C_{g,i}{}^{inlet}\widetilde{c}_{p,g}T_g{}^{inlet} = u|_{z=0}C_{g,i}\big|_{z=0}\widetilde{c}_{p,g}T_g\big|_{z=0} - \lambda\frac{\partial T_g}{\partial z}\Big|_{z=0} \quad (13)$$

$$z = L\frac{\partial T_g}{\partial z}\Big|_{z=L} = 0 \quad (14)$$

$$z = LP|_{z=L} = P^{out} \quad (15)$$

$$t = 0 C_{g,T}\big|_{t=0} = C_{g,He}{}^{inlet}$$

$$y_i|_{t=0} = 0$$

$$q_i^*\big|_{t=0} = 0 \quad (16)$$

$$t = 0 T_g\big|_{t=0} = T_g{}^{inlet}$$

$$T_w|_{t=0} = T_\infty \quad (17)$$

The mathematical model was solved with gPROMS® software (Process System Enterprise Inc., United Kingdom) using the orthogonal collocation on finite elements method (OCFEM) with third order polynomials and 25 intervals.

2.6. Model parameters

The affinity parameter of the Langmuir equation for component i was written as a function of the temperature as described by Do [63] (Equation (18).

$$b_i = b_{\infty,i}\exp\left(\frac{Q_i}{RT_g}\right) \quad (18)$$

where $b_{\infty,i}$ is the pre-exponential factor of the affinity parameter of component i and Q_i is the heat of adsorption of the Langmuir equation for component i.

Gas viscosity (μ) was estimated using the Wilke equation [61,64]. The axial mass dispersion coefficient of component i ($D_{ax,i}$) was estimated according to Edwards and Richardson [65] (Eq. (19)). For the mixture, the axial mass dispersion coefficient (D_{ax}) was calculated through a simple Kay's mixing rule [66].

$$D_{ax,i} = \frac{D_{m,i}}{\varepsilon}\left(0.73\varepsilon + \frac{0.5ReSc}{1+9.49(\varepsilon/ReSc)}\right);\ 0.008 < Re < 50 \quad (19)$$

where $D_{m,i}$ is the molecular diffusivity of each component i, estimated through Equation (20) as described by Ruthven [67].

$$D_{m,i} = \frac{1 - y_i}{\sum_{\substack{j=1\\ j\neq i}}^{n}\frac{y_j}{D_{ij}}} \quad (20)$$

where D_{ij} represents the binary diffusivity calculated using the Chapman-Enskog equation [61].

The film heat transfer coefficient was calculated according to Equation (21) [68]. The conductivity of the gas mixture (k_g) was calculated as reported by Bird *et al.* [61] using the feeding conditions and assuming them constant throughout the column. The overall heat transfer coefficient was estimated as per Equation 22 [69].

$$h_w = \frac{k_g}{d_p}\left(0.6Pr^{1/3}Re^{0.77}\right);\ 1 \le Re \le 40 \quad (21)$$

$$\frac{1}{U} = \frac{1}{h_w} + \frac{ed_i}{\lambda_w d_{ln}} + \frac{d_i}{d_{ex}h_{ex}};\ d_{ln} = \frac{d_{ex} - d_i}{\ln\left(\frac{d_{ex}}{d_{in}}\right)} \quad (22)$$

where λ_w is the thermal conductivity of the column wall, calculated according to Da Silva *et al.* [59]; h_{ex} is the external heat transfer coefficient, estimated using the correlation proposed by Churchill and Chu for a horizontal cylinder [69]; and d_{ex} is the column external diameter.

The specific heats of each component of the gas mixture at constant pressure and constant volume were obtained from Perry *et al.* [70].

2.7. Molecular simulation

The molecules of SO_2 and CO_2 were represented using the force fields of Ketko *et al.* [71] and TraPPE [72], respectively. In the model of SO_2, the oxygen and sulfur atoms were connected by bonds of 1.432 Å in length, in an angle of 119.3°, three Lennard-Jones centers and their respective point charges. Helium was represented by the united-atom

model proposed by Maitland *et al.* [73]. These models are known to accurately describe the vapor–liquid coexistence curves of the molecules and are commonly used in adsorption studies [74,75].

The most widely adopted carbon model in existing literature is the homogeneous slit-pore model. While the homogeneous model is able to successfully predict the CO_2 isotherm, it encounters limitations to predict the adsorption of SO_2, primarily due to its oversimplified uniformity of the slit walls. To address this issue, a novel slit-pore heterogeneous model (rMD) derived from reactive molecular dynamics [76–78] is introduced. The heterogeneous model, represented in Fig. 2, will be used for both gases. In section 3.5, a performance comparison is conducted between this homogeneous model and the heterogeneous model (rMD) for the prediction of single-component isotherms of CO_2 and SO_2.

The methodology of representative pores [79,80] was employed to select the most suitable pore sizes for studying the influence of SO_2 on CO_2 adsorption in individual pores.

The interaction energy between atoms was calculated using the 12–6 Lennard-Jones (LJ) potential plus the Coulomb potential (Equation (23).

$$U_{ij} = 4\varepsilon_{ij}\left[\left(\frac{\sigma_{ij}}{r_{ij}}\right)^{12} - \left(\frac{\sigma_{ij}}{r_{ij}}\right)^{6}\right] + \frac{q_i q_j}{4\varepsilon_0 r_{ij}} \quad (23)$$

where i and j are interacting atoms and r_{ij} is the distance between them. ε_{ij} and σ_{ij} are the LJ well depth and diameter, respectively. q_i and q_j are the partial charges of interacting atoms and ε_0 is the dielectric constant. Lorentz-Berthelot mixing rules were used to calculate the LJ cross parameters. Table 2 presents the force field parameters used in the simulations, where k_B is the Boltzmann constant.

2.8. Adsorption selectivity

Adsorption selectivity is a parameter frequently used to assess the separation efficiency [82]. It expresses the propensity of an adsorbent to selectively capture a specific component of the mixture in comparison to others. The adsorption selectivity of component i over component j (S_{ij}) was calculated from the adsorption capacity of each component in the mixture ($q_{i,mix}$), as shown in Equation (24).

$$S_{ij} = \frac{q_{i,mix} y_j}{q_{j,mix} y_i} \quad (24)$$

where y_i and y_j are the molar fractions at equilibrium of components i and j, respectively.

Given the difficulty in obtaining multicomponent adsorption experimental data, the IAST model has been frequently used to predict both the equilibrium and the selectivity in mixtures from single-component isotherms [1,83–87]. The suitability of the IAST model to predict the adsorption selectivity of the SO_2/CO_2 mixture in a fixed bed packed with the studied activated carbon sample has been evaluated. The adsorbed amounts of SO_2/CO_2 mixtures were estimated from the single-component equilibrium data following the methodology used by Do (1998) [63] and results were compared to the binary adsorption data obtained from the breakthrough curves and from the molecular simulations.

Table 2
Lennard-Jones force field parameters and point charges.

molecule	atom	σ(Å)	ε/k_B(K)	q(e)	bond distance (Å)
CO_2	C [a]	2.8	27	+ 0.7	1.16
	O [a]	3.05	79	− 0.35	–
SO_2	S [b]	3.39	73.8	+ 0.59	1.432
	O [b]	3.05	79	− 0.295	–
Carbon	C [c]	3.4	28	0	1.42

[a] TraPPE[72].
[b] Ketko *et al.*[71].
[c] Steele[81].

3. Results and discussion

3.1. Textural properties of the adsorbent

Table 3 shows the textural properties of the C141-S adsorbent, obtained from the N_2 isotherm at 77 K. Results indicate that the sample is essentially microporous, with a microporosity of 83 % [49,88] and exhibit textural properties which render it suitable for the adsorption of gases, such as high specific surface area and micropore volume [30,37,57,89]. A more detailed characterization of the sample can be found in Oliveira *et al.* [88].

3.2. Adsorption isotherms

In Figs. 3 and 4, the single-component adsorption isotherms of CO_2 and SO_2 are respectively shown for the sample C141-S at 303, 323 and 343 K, as well as their respective Langmuir fittings.

The behavior of the isotherms indicates that physical adsorption is

Table 3
Textural characteristics of C141-S activated carbon.

property	value
BET surface area (m^2/g)	1045
Total pore volume ($cm^3\ g^{-1}$)	0.45
Micropore volume ($cm^3\ g^{-1}$)	0.38
Microporosity (%)	83
Specific volume of solid ($cm^3\ g^{-1}$)	0.49

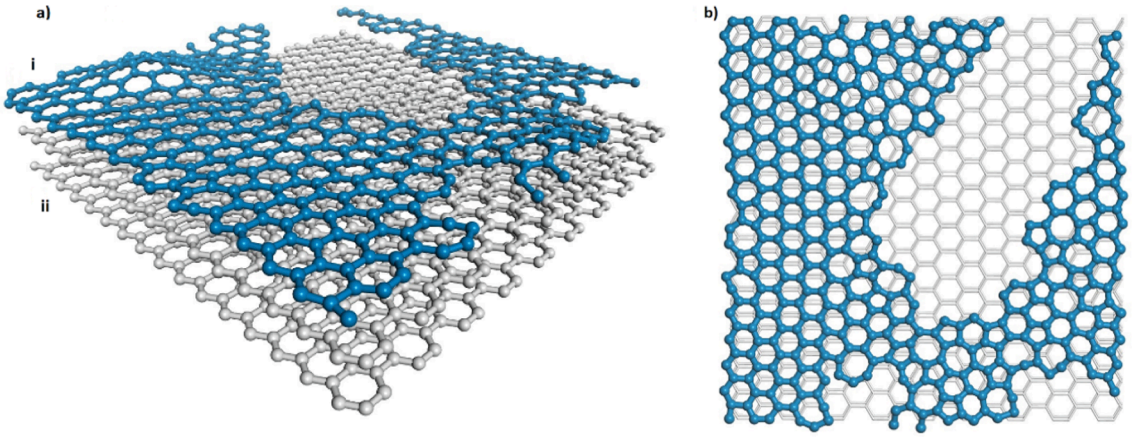

Fig. 2. Heterogeneous pore models (rMD): *i*-innermost wall and *ii*-outer wall (a). Graphene layer of the innermost wall with 25% of the oxidized carbon (b).

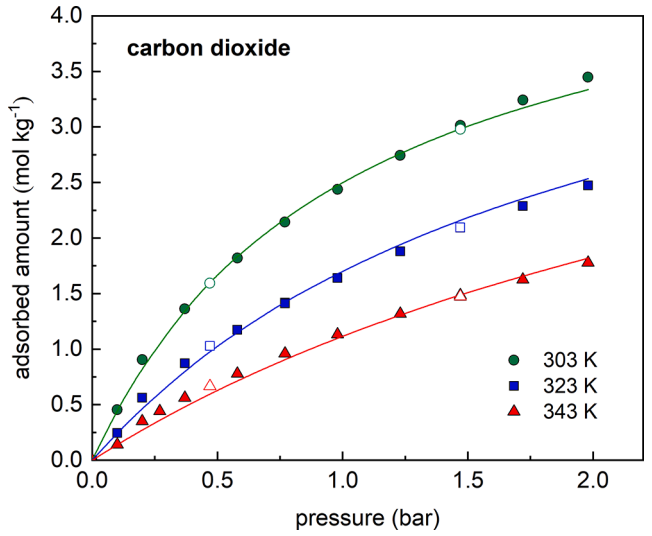

Fig. 3. Pure CO_2 adsorption isotherm on the C141-S activated carbon. Symbols: experimental data (solid. adsorption and open. desorption); Lines: Langmuir fit.

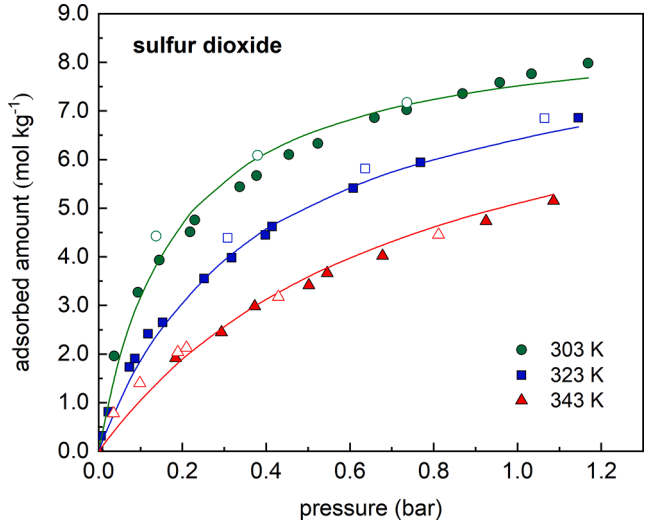

Fig. 4. Pure SO_2 adsorption isotherm on the C141-S activated carbon. Symbols: experimental data (solid – adsorption and open – desorption); Lines: Langmuir fit.

the predominant adsorption mechanism, since an increase in temperature promotes a decrease in the adsorbed concentration for both gases. This is due to the fact that, with increasing temperature, the molecules in the adsorbed phase achieve a sufficient energetic state to overcome the existing van der Waals forces and return to the fluid phase [89,90]. The desorption measurements presented in Figs. 3 and 4 indicate a complete reversibility of CO_2 isotherms and a slight hysteresis of SO_2 isotherms, especially at lower temperatures. Considering a cyclic separation process operated only by pressure/vacuum swing (PVSA), this suggests that even though SO_2 might build up in the pores over the adsorption–desorption cycles, depending on the pressure range applied and feed concentration, the sample presents a reasonable potential for long-term operation without the use of heat, as compared to zeolites or silicas [19], which might lose considerable capacity. The effects of the SO_2 hysteresis are further discussed in the next topic.

A distinct preferential adsorption for SO_2 over CO_2 is also observed from the isotherms, across the entire pressure range and for all temperatures under study. This is related to the fact that SO_2 has a critical temperature (T_c = 430 K), which is higher than that of CO_2 (T_c = 304 K). Thus, sulfur dioxide is more likely to behave as a condensable vapor than as supercritical gas, being relatively less volatile and more easily adsorbed. These observations are consistent with established literature. Dong *et al.* [91] and Mohammad and Sabeeh [92] have highlighted that gases with higher critical temperatures are associated with greater adsorption capacities when compared to gases with lower critical temperatures. Rios *et al.* [49,93] also corroborate this idea by explaining the enhanced adsorption of CO_2 over CH_4 and N_2, respectively, on activated carbons due to the substantially higher critical temperature of CO_2. This lower volatility is also associated to the hysteresis observed in the desorption branch of the SO_2 isotherms caused by the capillary condensation of the gas in the pores of the material. Furthermore, SO_2 has a higher permanent dipole moment and a high polarizability, as shown in Table 4. Such characteristics promote more intense dispersion interactions between the molecule and the surface of activated carbon, leading to higher adsorbed amounts in comparison to CO_2 [15,28,89,90,94,95]. Lastly, despite SO_2 being a larger molecule (kinetic diameter of 4.1 Å) than CO_2 (3.3 Å), both have suitable sizes for the adsorption in the pore structure of the activated carbon, given the topology of its microporous surface [2,31,88,96]. Oliveira *et al.* [88] reported a pore size distribution analysis on the C141-S activated carbon, revealing a predominant occurrence of pores ranging from 3 to 16 Å within its microporous structure. This characterization provides valuable insights into the capacity of the adsorbent material to accommodate molecules of various sizes, such as CO_2 and SO_2.

Table 5 shows the calculated parameters of the Langmuir equation as a function of temperature (q_{max}, b_∞ and Q) along with the isosteric enthalpy of adsorption (ΔH_i^{iso}) for each component of the mixture. Parameter q_{max} is the maximum adsorption capacity of the adsorbent and parameter b represents how strongly an adsorbate molecule is attracted to the adsorbent surface [63,96]. All parameters presented higher values for SO_2 in relation to CO_2, as expected from the isotherms. Regarding the Langmuir fit to the experimental data, the correlation coefficients (R^2) were greater than 0.99 for both components.

The isosteric enthalpy of adsorption provides information about the extent of the thermal effects within the bed during the adsorption and desorption steps, indicating the minimum energy requirement for the adsorbed molecule to return to the fluid phase [97]. The higher isosteric enthalpy of adsorption of SO_2 also evidences the higher affinity of the adsorbent for sulfur dioxide, which means a higher energy penalty for its desorption. The values obtained for both components are in agreement with data reported in the literature for activated carbons [1,49,90,98] and other materials such as zeolites [31] and MOFs [2,26,28,58,95].

3.3. Breakthrough curves

Figs. 5 and 6 show the single-component breakthrough curves of CO_2 and SO_2 (both in He), respectively, under the conditions specified in Table 1, along with the respective simulations. The curves are step-shaped with apparent low mass transfer resistance and adsorption capacities in agreement with the literature for activated carbon [89,90,94,99]. The higher adsorption capacity of SO_2 observed in the isotherms is also corroborated by its higher retention times.

Results show a satisfactory match between experimental and simulated data, indicating the suitability of the mathematical model to describe the dynamic behavior of single-component adsorption of CO_2 and SO_2 in a fixed bed, which allows for its use in the analysis of

Table 4
Physical properties of CO_2 and SO_2.

properties	SO_2	CO_2
Dipole moment (D)	1.633	–
Quadrupole moment (a.u.)	3.3	3.2
Polarizability (a_0^3)	26	18

Source: Adapted from Li *et al.* [95].

Table 5
Parameters of the Langmuir equation as a function of temperature along with isosteric enthalpy of adsorption for each adsorbate.

parameters	SO_2	CO_2
q_{max}(mol kg^{-1})	8.83	5.03
b_∞(Pa^{-1})	3.1×10^{-10}	2.2×10^{-10}
Q(kJ/mol)	30.59	26.98
$R2$	0.9978	0.9969
ΔH_i^{iso}(kJ/mol)	30.60	26.97

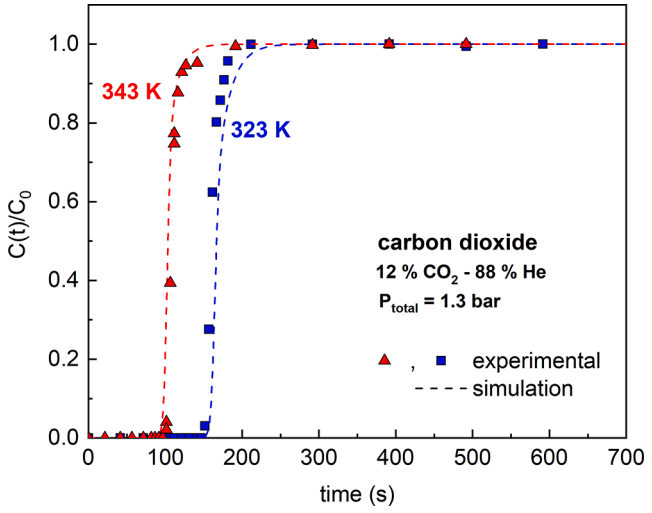

Fig. 5. Breakthrough curves of CO_2 in He (12 % v/v CO_2 and 88 % v/v He) on C141-S activated carbon at temperatures of 323 and 343 K.

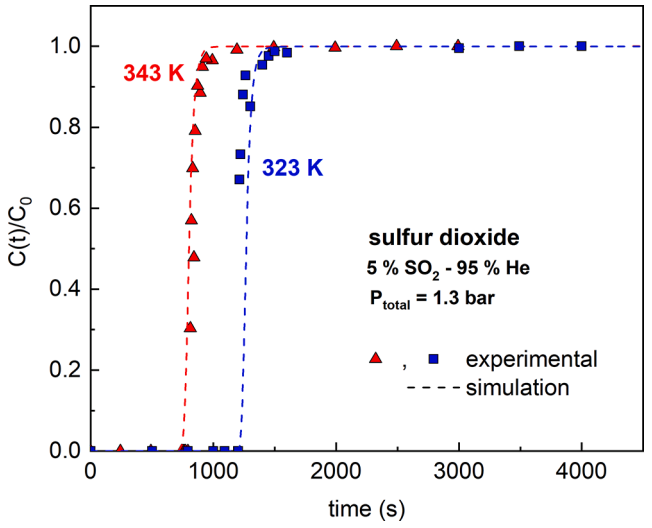

Fig. 6. Breakthrough curves of SO_2 in He (5 % v/v SO_2 and 95 % v/v He) on C141-S activated carbon at temperatures of 323 and 343 K.

different conditions. The diffusion parameter D_μ/r_μ^2, estimated by fitting the model to the experimental breakthrough curves was 0.216 s^{-1} for CO_2 and 0.045 s^{-1} for SO_2, which are in the same order of magnitude of those reported in the literature [49,99–101] for activated carbons, suggesting that the LDF approximation is suitable for the studied system. This parameter presented no significant change within the studied temperature range for each gas, which has also been observed in other studies [49,99]. The relationship between the values of D_μ/r_μ^2 obtained for CO_2 and SO_2 is also in good agreement with the literature [94].

The dynamics of multicomponent adsorption for a feed containing 12 % v/v CO_2 + 5 % v/v SO_2 diluted in He was also evaluated at 323 K and 1.3 bar, as shown in Fig. 7. Table 6 summarizes the parameters used in the simulation.

While CO_2 breaks through the column significantly earlier, SO_2 is only detected much later at the outlet, with a nearly 10 times larger breakpoint. There is a clear competition of the two gases for some of the adsorption sites, which explains the overshoot behavior observed for CO_2, indicating its displacement by SO_2.

From the multicomponent breakthrough curves (Fig. 7), the calculated adsorbed amount of carbon dioxide was 0.294 mol kg^{-1} whereas a total amount of sulfur dioxide of 1.64 mol kg^{-1} was retained by the bed. In comparison to the single-component breakthrough curve, the capacity of CO_2 is reduced by approximately 46 % (from 0.548 to 0.294 mol kg^{-1}) under the same conditions, indicating a severe negative impact of SO_2 on CO_2 capture.

Regarding the simulation results, it noteworthy that the model was able to satisfactorily predict the breakpoint for both gases, the kinetics and also the complete overshoot observed of the less adsorbed component. This demonstrates that the implemented model provides reliable results and can be used to describe the behavior of the system under different conditions of pressure, temperature and concentration.

The desorption of both components was also experimentally evaluated in order to assess the regeneration requirements and suitability of the sample for an application on CO_2 capture by cyclic adsorption processes in the presence of sulfur dioxide. After saturating the bed with the mixture (as in Fig. 7), the feed is switched to pure helium flowing at 83 mL min^{-1} under isothermal conditions. The helium flow purges the gases from the column and the area under the concentration curves allows to determine the amount of each gas leaving the column in this step [51]. Subsequently, to verify the existence of remaining adsorbed components, the system was submitted to a temperature ramp of 3 K min^{-1} up to 423 K while the concentrations of both components were monitored until they were no longer detected. Fig. 8 shows the desorption curves obtained using the elution with He (Fig. 8 – step B) and using the temperature ramp (Fig. 8 – step C).

In Fig. 8 – step B, an immediate decrease in the concentration of both components inside the bed is observed. It is noteworthy that a simple decrease in the partial pressure of CO_2 by He elution is sufficient to remove practically all adsorbed molecules of the gas from the bed. The same is not observed for sulfur dioxide, which presents a more disperse concentration front along the time. This fact confirms the stronger adsorbent–SO_2 interactions and the need of additional energy (*i.e.*, heat)

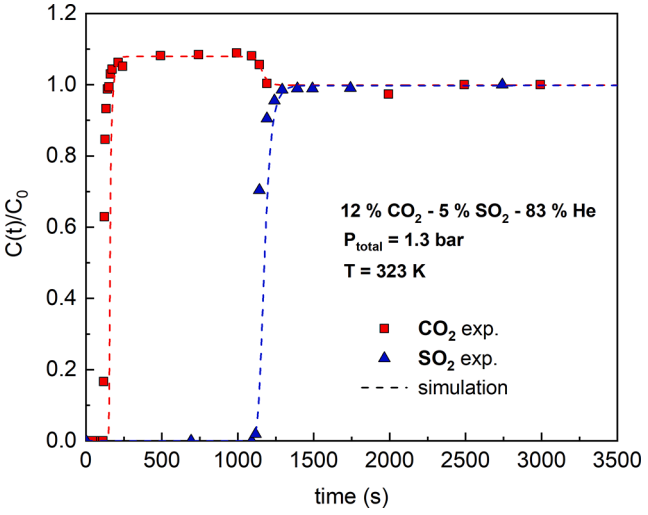

Fig. 7. Breakthrough curve of CO_2-SO_2 in He (12 % v/v CO_2, 5 % v/v SO_2, 83 % v/v He) at 323 K and 1.3 bar on C141-S activated carbon. Symbols are experimental data and lines are simulated data.

Table 6
Model parameters used in the simulation of the CO_2-SO_2 system at 323 K and 1.3 bar on C141-S activated carbon.

model parameters	
bed/column	
d_{in}(m)	0.005
L(m)	0.25
α_w(m^{-1})	833
α_{wL}(m^{-1})	991
ε	0.57
ρ_b(kg m^{-3})	465
ρ_w(kg m^{-3})	7833
particle	
r_p(m)	3.99×10^{-4}
ρ_p(kg m^{-3})	1053
ε_p	0.48
mass transfer	
D_{ax}(m^2/s)	5.10×10^{-5}
$D_c/r_c^2 - CO_2$(s^{-1})	0.06
$D_c/r_c^2 - SO_2$(s^{-1})	0.046
energy transfer	
$\widetilde{c}_{p,g}$(J mol^{-1} K^{-1})	23.97
$\widetilde{c}_{v,g}$(J mol^{-1} K^{-1})	15.67
$\widetilde{c}_{v,g,CO_2}$(J mol^{-1} K^{-1})	29.76
$\widetilde{c}_{v,g,SO_2}$(J mol^{-1} K^{-1})	34.85
$\widetilde{c}_{v,g,He}$(J mol^{-1} K^{-1})	12.47
$\widehat{c}_{p,w}$(J kg^{-1} K^{-1})	502.08
k_g(W m^{-1} K^{-1})	0.10
h_w(W m^{-2} K^{-1})	75.82
U(W m^{-2} K^{-1})	0.06
λ(W m^{-1} K^{-1})	0.76
momentum transfer	
u^{inlet}(m/s)	0.078
P^{out}(bar)	1.31
μ(Pa s)	2.09×10^{-5}

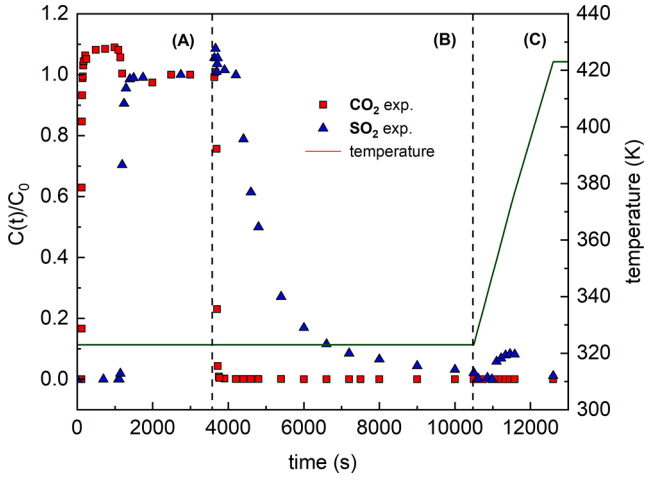

Fig. 8. Concentration histories of CO_2-SO_2 in He (12% v/v CO_2, 5% v/v SO_2, 83% v/v He) for (A) the adsorption step, (B) desorption step using elution with He and (C) desorption step using a temperature ramp.

Table 7
Calculated adsorbed and desorbed amounts for SO_2 in the fixed bed experiments for the CO_2-SO_2 system.

component	step	adsorbed/desorbed concentration (mol kg^{-1})
SO_2	(A)	1.640
	(B)	1.531
	(C)	0.121

to remove the gas molecules from the sample, allowing a complete regeneration. Table 7 shows the calculated amounts adsorbed (step A) and desorbed (steps B and C) of sulfur dioxide from the curves presented in Fig. 8.

In the case of sulfur dioxide, the elution with He (step B) is able to remove approximately 93 % of the molecules retained in the bed, requiring an additional step to remove the remaining SO_2. The data in Table 7, as calculated from mass balances, confirms that, only after heating the sample (step C), SO_2 is totally desorbed. It is evident that heat is necessary to remove the remaining SO_2, which could build up in a long-term pressure-swing cyclic operation decreasing the CO_2 capture efficiency. Although all SO_2 adsorbed could be recovered, it was not possible to confirm or refute an eventual capacity loss of the sample. Note that no reactions are likely to take place under the studied conditions and no extraneous signals have been detected by the chromatograph during the heating step. Besides, the experiments with SO_2 using the same packed bed have shown very good repeatability. These results suggest that activated carbons are potentially suitable for CO_2 capture in the presence of SO_2 via cyclic adsorption processes combining pressure (or vacuum) and temperature swings.

3.4. Impact of SO_2 on CO_2 retention capacity

Considering that SO_2 concentration in flue gases typically ranges from 500 to 5000 ppmv [18], the validated mathematical model was used to simulate the capture process at such conditions and to evaluate the impact of SO_2 on the CO_2 retention capacity.

The effects of SO_2 were assessed by simulations at $T = 323$ K and $P_{total} = 1.3$ bar for three additional gas feeds, with SO_2 concentrations of 2 % v/v, 5 000 ppmv and 2 000 ppmv diluted in He, as shown in Table 8. All other parameters were the same used to describe the experimental data.

Fig. 9 presents the results obtained for the carbon dioxide retention capacity normalized to the capacity of the single-component CO_2 experimental data (feed A) as a function of the concentration of sulfur dioxide in the mixture. Results confirm a severe and continuous decrease in the CO_2 retention capacity as SO_2 feed concentration increases. The competition for adsorption sites is relevant even at the lowest tested SO_2 concentration (feed B), leading to a capacity loss of about 5.8 %. Although CO_2 concentration is about 60 times higher than that of SO_2 (12:0.2 – feed B), the stronger interactions of SO_2 molecules with the adsorbent are capable of reducing the CO_2 uptake that much. The highest concentrations of SO_2 (cases D and E) substantially affect the CO_2 retention capacity, leading to CO_2 capacity loss of approximately 24 % and 46 %.

Regarding the typical concentration ranges in exhaust gases, represented by feeds B and C, the observed capacity losses are about 5.8 and 9.3 %, respectively. Czyżewski *et al.* [33] report a decrease of up to 88 % in CO_2 retention capacity of activated carbon samples containing CaO and MgO when exposed to a SO_2 concentration of 2 000 ppmv at a similar temperature (318 K). In another study by Sanz-Pérez *et al.* [19] a decrease in CO_2 retention capacity of up to 61 % is reported for an amino-functionalized SBA-15 when submitted to a SO_2 concentration of 1000 ppmv also at a similar temperature (318 K). A simple comparison with the results obtained in this work suggests that sulfur dioxide has a

Table 8
Feed compositions used to estimate the impact of SO_2 on CO_2 retention capacity at 323 K and 1.3 bar on C141-S activated carbon.

feed	composition	source
A	12 % CO_2 + He	experimental
B	12 % CO_2 + 2 000 ppmv SO_2 + He	simulation (mathematical model)
C	12 % CO_2 + 5 000 ppmv SO_2 + He	simulation (mathematical model)
D	12 % CO_2 + 2 % SO_2 + He	simulation (mathematical model)
E	12 % CO_2 + 5 % SO_2 + He	experimental

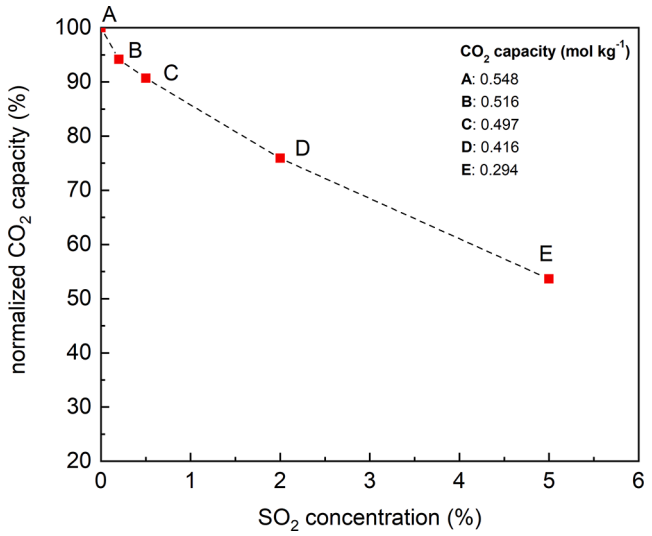

Fig. 9. Adsorbed amounts of CO_2 calculated from the breakthrough curves obtained for different feed conditions.

relatively lower impact on the CO_2 retention capacity using non-impregnated or non-modified carbon-based materials, such as the C141-S. Combined to the fact that both gases can be completely desorbed under appropriate conditions, the results suggest that CO_2 capture in post-combustion conditions can be performed in a single operation, ruling out the need of a pre-treatment unit for the removal of SO_2 [102]. For CO_2 capture by VPSA (Vacuum Pressure Swing Adsorption) processes, literature reports that the installation of a pre-treatment section for SO_2 removal tends to be less costly than accepting the degradation of the adsorbent capacity in cases where the sulfur dioxide is present in the flue gas [17,22]. Therefore, even though SO_2 was found to cause little interference in the CO_2 retention capacity at typical concentrations and there is no clear evidence of adsorbent degradation, the analysis of the feasibility of operating in a single-unit might require further investigation of possible poisoning/deactivation of adsorption sites and loss of capacity over several adsorption/desorption cycles [19,27,34].

3.5. Molecular simulation

3.5.1. Validation

Fig. 10 shows the experimental and simulated single-component CO_2 and SO_2 isotherms at 323 K. The graphs are in log scale to highlight the low loading range. It is evident that the homogeneous slit-pore carbon model (depicted by the blue line) cannot accurately reproduce the SO_2 isotherm. In contrast, the heterogeneous model (indicated by the orange line) describes much better the SO_2 experimental isotherms (depicted by black circles), which were obtained by gravimetry (Figs. 2 and 3). The experimental data extracted from breakthrough curves are represented by the empty triangles.

Details of the heterogeneous rMD model, in contrast with the conventional homogeneous model, isotherm calculations and the representative pore methodology are found in Montenegro *et al.* [103]. Table 9 presents a comparison of uptakes measured experimentally with those obtained from molecular simulation, evidencing the suitability of the rMD model for reproducing experimental data.

3.5.2. Deactivation of individual pores

Following the validation of the models, we investigated the individual behavior of the CO_2 and SO_2 mixture within selected representative pores (Fig. 11). It was found that the 7 Å pore was notably affected by the presence of SO_2 (Fig. 11a). At 5 000 ppmv SO_2, this pore experienced deactivation over 8 %, and at 50 000 ppmv, it underwent a deactivation exceeding 50 %. These figures strongly suggest a competitive interaction between SO_2 and CO_2 molecules.

The enthalpies of adsorption for the different representative pores, as calculated at 323 K and 1 kPa (Table 10), indicate that in the 7 Å pore, SO_2 exhibits a more pronounced interaction with the pore surface, as compared to CO_2. Consequently, it takes priority in occupying the pore volume. Given the limited accessible volume in the 7 Å pore (capable of accommodating only one layer of molecules), SO_2 molecules swiftly occupy the adsorption sites, leading to the inactivation of the pore for CO_2 adsorption.

While assessing adsorption within the 8.9 Å pore (as illustrated in Fig. 11b), a surprising phenomenon emerged: the adsorbed amount of CO_2 increased with the concentration of SO_2 in the mixture, even up to

Table 9
Adsorbed amounts of CO_2 and SO_2 diluted in He at 323 K and 1.3 bar on carbon C141-S calculated according to the homogeneous slit-pore and rMD models.

	CO_2 uptake (mol kg^{-1}) (12 % CO_2 + 88 % He) @ 323 K and 1.3 bar	**SO_2 uptake (mol kg^{-1})** (5 % SO_2 + 88 % He) @ 323 K and 1.3 bar
molecular simulation		
homogeneous model	0.37	1.4
rMD model	0.54	1.56
experimental		
breakthrough curves	0.548	1.667
isotherms	0.49	1.63

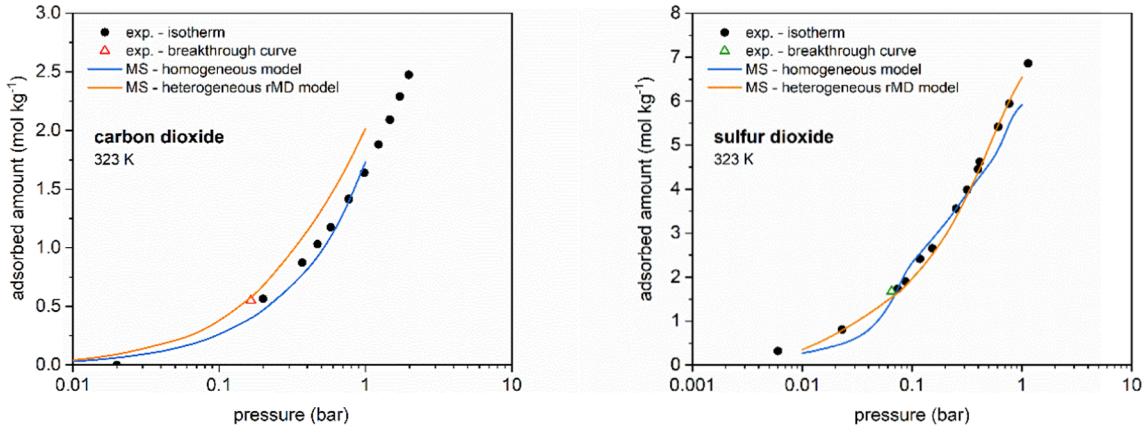

Fig. 10. Single-component adsorption isotherms at 323 K predicted by the homogeneous model and the heterogeneous rMD model (lines): (a) CO_2 and (b) SO_2. The experimental isotherms from Figs. 2 and 3 (black circles) and the values of adsorption from the breakthrough curves in Figs. 4 and 5 (empty triangles) are also presented.

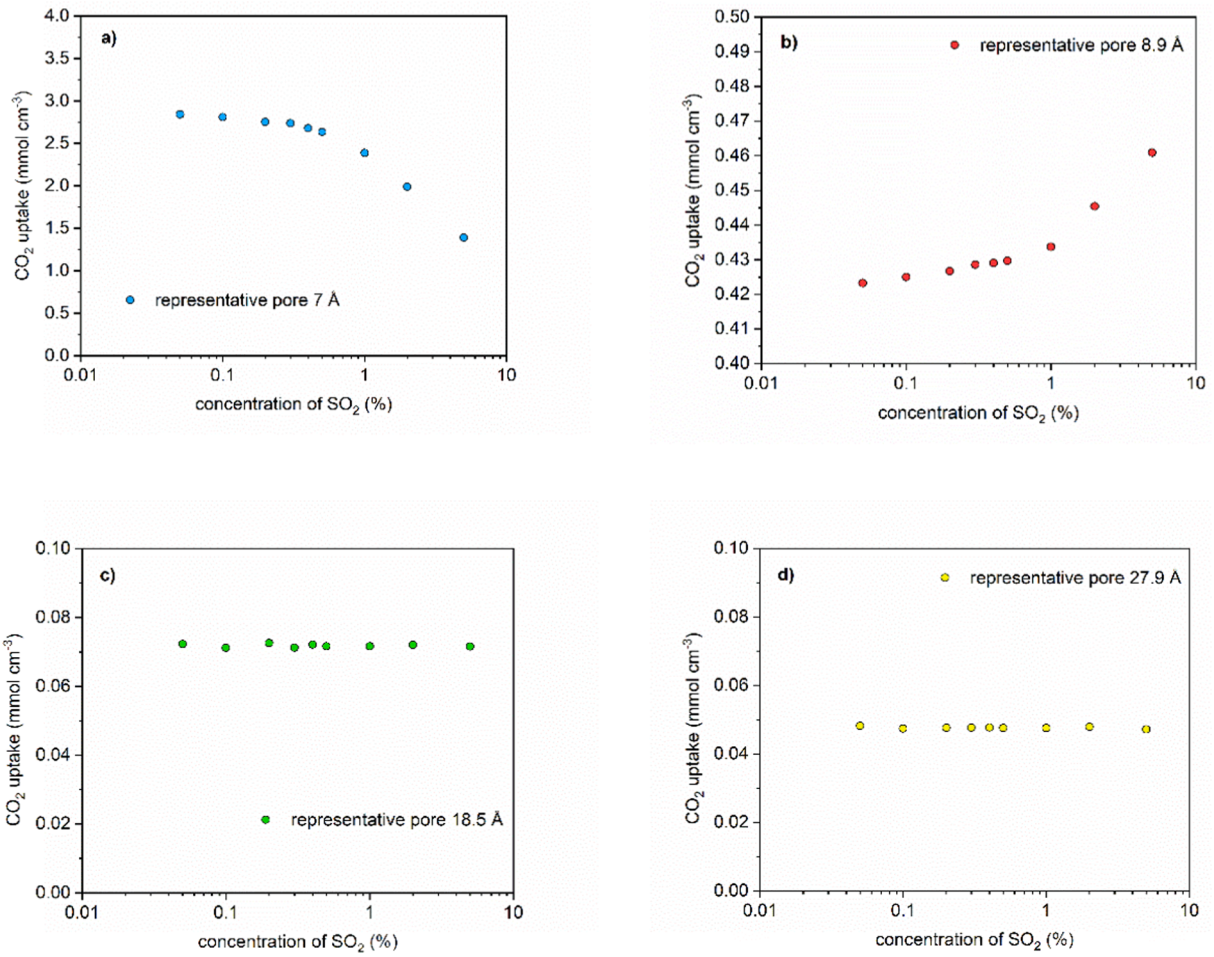

Fig. 11. Theoretical adsorbed amounts of CO_2 in the mixture containing 12 % CO_2 + He + varying SO_2 concentration at 323 K and 1.3 bar in the heterogeneous rMD pores.

Table 10
Enthalpy of adsorption in heterogeneous pores rMD calculated for CO_2 and SO_2 at 323 K and 1 kPa.

pore size (Å)	enthalpy of adsorption (kJ/mol)	
	CO_2	SO_2
7	−28.08	−38.20
8.9	−18.13	−22.50
18.5	−14.96	−16.86
27.9	−14.21	−16.47

Table 11
Loading of CO_2 and SO_2 (molecules per pore) for the mixture with 12 % CO_2 + SO_2 + He at 323 K and 1.3 bar.

% SO_2	7 Å		8.9 Å	
	CO_2molecules/pore	SO_2molecules/pore	CO_2molecules/pore	SO_2molecules/pore
5	6.37	24.53	2.96	8.59
2	9.11	14.27	2.86	2.64
0.5	12.06	4.11	2.75	0.58
0.4	12.27	3.35	2.75	0.46
0.3	12.54	2.50	2.75	0.34
0.2	12.62	1.62	2.74	0.22
0.1	12.88	0.80	2.72	0.11
0.05	13.02	0.40	2.71	0.0
0	13.13	0	2.72	0

50,000 ppmv. CO_2 uptake increased approximately 2 % at 5000 ppmv of SO_2 and nearly 9 % at 50,000 ppmv. These counterintuitive finding suggests the existence of a cooperative effect in which the presence of SO_2 molecules enhances the adsorption of CO_2.

The difference in the filling regime of the 7 and 8.9 Å pores is evident in Table 11. In the absence of SO_2, the 7 and 8.9 Å pores adsorb 13.13 and 2.72 molecules of CO_2 respectively. For the 7 Å pore, as the concentration of SO_2 increases, a decrease in the adsorbed amount of CO_2 is observed, reaching just 6.37 molecules at 5 % SO_2 in the mixture, less than half of the amount adsorbed in the absence of SO_2. Conversely, in the 8.9 Å pore, the adsorbed amount of CO_2 increases, reaching 2.96 molecules/pore when SO_2 concentration is 5 %.

To further investigate this phenomenon, the energy distribution of one CO_2 molecule within the 8.9 Å was calculated according to the rMD slit-pore model and compared to the distribution within the same pore containing one CO_2 molecule and eight SO_2 molecules. These simulations were carried out using the canonical ensemble (NVT), with the number of SO_2 molecules inserted corresponding to the amount adsorbed in the mixture containing 12 % CO_2 + 5 % SO_2 + He at 323 K and 1.3 bar. Fig. 12a presents the two distributions obtained.

The presence of SO_2 molecules within the pore shifted the energy distribution toward higher values, approximately from 5 to 6 kcal mol^{-1}. The SO_2 molecules ultimately enhanced the adsorption of CO_2 through the fluid–fluid potential (SO_2-CO_2). Fig. 12b illustrates the system and its configuration. This cooperative effect mirrors what was previously observed for the H_2S-CO_2 interaction in the 8.9 Å homogeneous slit-pore [74].

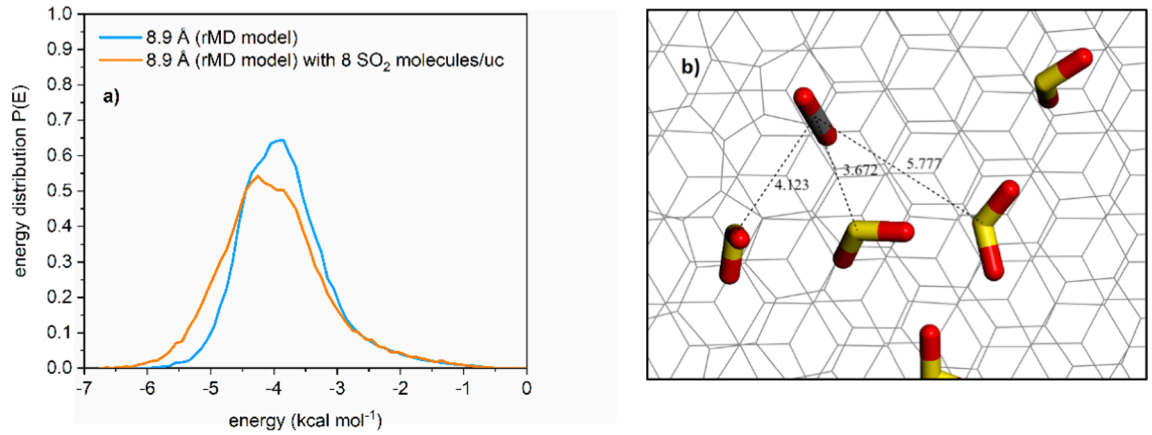

Fig. 12. (a) Energy distribution of a CO_2 molecule in the 8.9 Å rMD slit-pore without SO_2 molecules (blue line) and with SO_2 molecules (orange line). (b) Snapshot of enhanced CO_2 interaction in the presence of SO_2 molecules (red: oxygen, gray: carbon, yellow: sulfur). (For interpretation of the references to colour in this figure legend, the reader is referred to the web version of this article.)

The adsorbed amounts of CO_2 in larger pores – 18.5 and 27.9 Å (as shown in Fig. 10c and d) - remained constant despite increasing SO_2 concentration. This behavior can be attributed to the minimal difference in enthalpies of adsorption between both species and the low adsorbed amounts. Consequently, there is no significant competition for adsorption sites within these representative pores.

3.5.3. Global deactivation

Simulations were performed to investigate the adsorption of the series of mixtures examined in the preceding sections. These mixtures consisted of 12 % CO_2 with varying concentrations of SO_2, ranging from 500 to 5 000 ppmv, diluted in helium (He) at 323 K and 1.3 bar. These simulations were conducted within the same four selected representative pores (7, 8.9, 18.5, and 27.9 Å) using the rMD model. Additionally, the assessment was extended to encompass the upper limit concentration of 50 000 ppmv of SO_2.

Fig. 13 and Table 12 offer insights into the deactivation of the adsorbent, quantifying the extent to which the capacity for CO_2 adsorption is reduced in the presence of SO_2, as calculated according to Eq. (25).

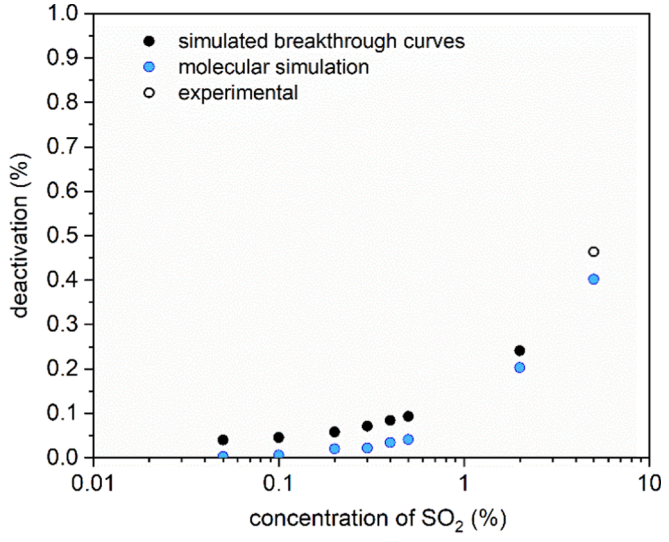

Fig. 13. Deactivation of CO_2 adsorbed on C141-S carbon as a function of SO_2 concentration in the mixture with 12 % CO_2 + He at 323 K and 1.3 bar. Calculations are based in mathematical model of the column dynamics (full black circles), molecular simulation of the mixtures (light blue circles) and experimental breakthrough data (empty black circle). (For interpretation of the references to colour in this figure legend, the reader is referred to the web version of this article.)

Table 12
Sample deactivation for CO_2 adsorption in mixtures with SO_2 estimated from column dynamics and molecular simulation.

SO_2 (%)	column dynamics (%)	molecular simulation (%)
0.05	4.0	0.3
0.1	4.6	0.6
0.2	5.8	2.0
0.3	7.1	2.2
0.4	8.4	3.5
0.5	9.3	4.1
2	24.1	20.3
5	46	40.2

$$\text{deactivation}(\%) = 1 - \frac{q_{CO_2,mix}}{q_{CO_2}} \quad (25)$$

where $q_{CO_2,mix}$ is the adsorbed amount of CO_2 in the mixture with SO_2 and q_{CO_2} is the adsorbed amount of pure CO_2. Calculations were performed across a range of mixtures, ranging from 0.05 to 50 000 ppmv of SO_2 and the results were compared to the data obtained from column dynamics (experiments and simulations), shown in Fig. 9.

Both curves in Fig. 13 exhibit remarkably similar trends. Notably, the mathematical model yields a higher level of deactivation than the molecular simulation within the low loading range (up to 0.5 %). As the SO_2 concentration increases, the discrepancy between the values estimated by the mathematical model and those from the molecular simulation diminishes. At concentrations of 2 % and 5 %, the values derived from the mathematical model and molecular simulation are nearly identical, indicating that the carbon can be deactivated by 40 % to 46 % of its original capacity (pure CO_2).

The more pronounced disparity in the low loading region can be attributed to the simplifications inherent to the Langmuir model and the IAST theory, both of which do not properly account for competitive effects and lateral molecular interactions between CO_2 and SO_2. These effects become more prominent in the low loading region due to competition among the most energetically favorable sites, characterized by increased heterogeneity. It is precisely this type of interaction that the Langmuir + IAST models fail to incorporate.

3.5.4. Selectivity

The selectivity of SO_2 over CO_2 was computed for the carbon sample at 323 K and 1.3 bar. Fig. 14 illustrates the theoretical selectivity of SO_2

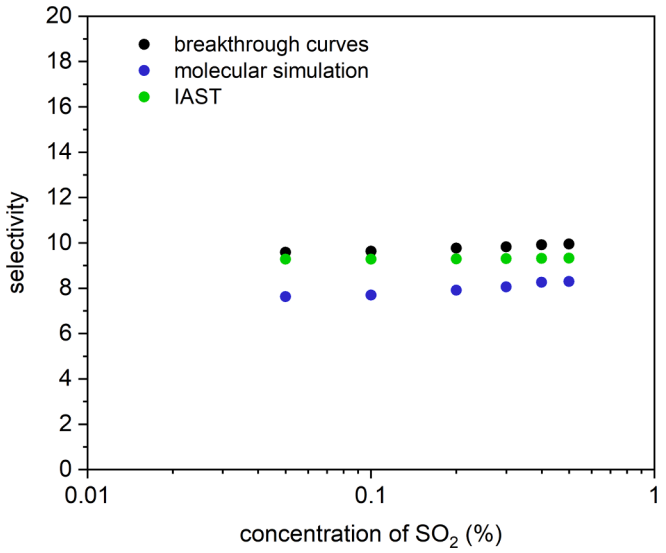

Fig. 14. Selectivity of SO_2 in relation to CO_2 in the mixture with 12 % CO_2 + SO_2 + He at 323 K and 1.3 bar.

in C141-S concerning the concentration of SO_2 in the mixture with 12 % CO_2 + He. The predictions calculated using the mathematical model and IAST are also presented. Selectivity experiences a slight increase with the rising concentration of SO_2 in the mixture, up to 5 000 ppmv. Molecular simulation suggests selectivity values around 8, while the mathematical model and IAST suggest values hovering around 9. This discrepancy can be attributed to the simplifications embedded in the isotherm models employed in the mathematical model, as previously discussed.

4. Conclusions

The presence of SO_2 at typical flue gas concentrations (up to 0.5 %) is likely to have little influence on the CO_2 retention capacity in non-impregnated carbon-based materials. The evaluated material presented a decrease of only 2 to 5.8 % in the amount adsorbed of CO_2 for a SO_2 concentration of 2 000 ppmv. Combining such a limited impact on the CO_2 retention capacity with the possibility of complete regeneration of the material (the adsorption of both components appears to be predominantly physical), it is possible to carry out a capture process in a single stage/equipment, without the need for a pre-treatment unit for the SO_2 removal. Although unlikely to occur in the studied carbon, potential deactivation effects must be carefully considered for long-term cyclic processes.

A mathematical model coupling differential mass, energy and momentum balances with the equilibrium described by the extended Langmuir model and kinetics described by the LDF approach is able to satisfactorily describe both single and multicomponent adsorption of SO_2 and CO_2 in a fixed bed.

A new, more realistic carbon heterogeneous model, was used to predict the adsorption of pure components and mixtures by molecular simulation with excellent agreement between experimental and simulated data. The molecular simulation of the adsorption of the mixture of CO_2 and SO_2, in individual pores, revealed a surprising cooperative effect between the CO_2 and SO_2 molecules for the 8.9 Å pore, where small concentrations of SO_2 enhance the adsorption of more CO_2. The 7 Å pore showed the most severe deactivation and pores of 18.5 and 27.9 Å were indifferent to the presence of SO_2. This discovery holds potential for the development of materials designed for more efficient carbon capture from flue gases despite the presence of SO_2.

The IAST and the Langmuir Extended models showed discrepancies, as compared with the molecular simulation model, suggesting caution when applying them for systems with SO_2 and CO_2 in the low loading range (up to 0.5 %). The in-depth study of adsorption in individual pore sizes shows promise of guiding the synthesis of carbons with optimized performance for CO_2 capture in streams contaminated with SO_2.

Author contributions

Davi D. S. Moreira: Software, Validation, Investigation, Writing - Original Draft, Visualization. **Daniel V. Gonçalves:** Methodology, Software, Validation, Visualization. **Juliana A. Coelho:** Validation, Supervision. **Diana C. S. de Azevedo:** Conceptualization, Writing - Review & Editing, Funding acquisition. **Rafael B. Rios:** Conceptualization, Software, Validation, Writing - Original Draft, Supervision **Sebastião M. P. de Lucena:** Conceptualization, Methodology, Writing - Review & Editing, Visualization, Supervision. **Moises Bastos-Neto:** Conceptualization, Validation, Writing - Original Draft, Writing - Review & Editing, Visualization, Project administration, Funding acquisition

CRediT authorship contribution statement

Davi D.S. Moreira: Investigation, Software, Validation, Visualization, Writing – original draft. **Daniel V. Gonçalves:** Methodology, Software, Validation, Visualization. **Juliana A. Coelho:** Supervision, Validation. **Diana C.S. de Azevedo:** Conceptualization, Funding acquisition, Writing – review & editing. **Rafael B. Rios:** Conceptualization, Software, Supervision, Validation, Writing – original draft. **Sebastião M.P. de Lucena:** Conceptualization, Methodology, Supervision, Visualization, Writing – review & editing. **Moises Bastos-Neto:** Conceptualization, Funding acquisition, Project administration, Validation, Visualization, Writing – original draft, Writing – review & editing.

Declaration of Competing Interest

The authors declare that they have no known competing financial interests or personal relationships that could have appeared to influence the work reported in this paper.

Data availability

Data will be made available on request.

Acknowledgements

The authors acknowledge the financial support from Coordenação de Aperfeiçoamento de Pessoal de Nível Superior (CAPES) and Conselho Nacional de Desenvolvimento Científico e Tecnológico (CNPq).

References

[1] J.G. Bell, M.J. Benham, K.M. Thomas, Adsorption of carbon dioxide, water vapor, nitrogen, and sulfur dioxide on activated carbon for capture from flue gases: competitive adsorption and selectivity aspects, Energy Fuel 35 (9) (2021) 8102–8116.
[2] P. Brandt, et al., Comparative evaluation of different MOF and Non-MOF Porous Materials for SO2 adsorption and separation showing the importance of small pore diameters for low-pressure uptake, Adv. Sustain. Syst. 5 (4) (2021) 2000285.
[3] F. Adedoyin, et al., Structural breaks in CO2 emissions: Are they caused by climate change protests or other factors? J. Environ. Manage. 266 (2020) 110628.
[4] K.N. Finney, et al., Chapter 2 - Carbon capture technologies, in Bioenergy with Carbon Capture and Storage, J.C. Magalhães Pires and A.L.D. Cunha Gonçalves, Editors. 2019, Academic Press. p. 15-45.
[5] F. Syed, A. Ullah, Estimation of economic benefits associated with the reduction in the CO2 emission due to COVID-19, Environmental Challenges 3 (2021) 100069.
[6] IEA, World Energy Outlook, 2018, IEA, Paris, 2018.
[7] C. Chao, et al., Post-combustion carbon capture, Renew. Sustain. Energy Rev. 138 (2021) 110490.
[8] Z. Liang, et al., Recent progress and new developments in post-combustion carbon-capture technology with amine based solvents, Int. J. Greenhouse Gas Control 40 (2015) 26–54.

[9] M. Wang, et al., Process intensification for post-combustion CO2 capture with chemical absorption: A critical review, Appl. Energy 158 (2015) 275–291.
[10] K. Ge, et al., Modeling CO2 adsorption dynamics within solid amine sorbent based on the fundamental diffusion-reaction processes, Chem. Eng. J. 364 (2019) 328–339.
[11] M. Khnifira, et al., Combined DFT and MD simulation approach for the study of SO2 and CO2 adsorption on graphite (111) surface in aqueous medium, Curr. Res. Green Sustain. Chem. 4 (2021) 100085.
[12] M.A. Quader, S. Ahmed, Chapter Four - Bioenergy With Carbon Capture and Storage (BECCS): Future Prospects of Carbon-Negative Technologies, in Clean Energy for Sustainable Development, M.G. Rasul, A.k. Azad, and S.C. Sharma, Editors. 2017, Academic Press. p. 91-140.
[13] S. Divekar, et al., Improved CO2 recovery from flue gas by layered bed Vacuum Swing Adsorption (VSA), Sep. Purif. Technol. 234 (2020) 115594.
[14] B. Gimeno, et al., Influence of SO2 on CO2 storage for CCS technology: Evaluation of CO2/SO2 co-capture, Appl. Energy 206 (2017) 172–180.
[15] L. Luo, et al., Adsorption species distribution and multicomponent adsorption mechanism of SO2, NO, and CO2 on commercial adsorbents, Energy Fuel 31 (10) (2017) 11026–11033.
[16] C. Kim, W. Choi, M. Choi, SO2-resistant amine-containing CO2 adsorbent with a surface protection layer, ACS Appl. Mater. Interfaces 11 (18) (2019) 16586–16593.
[17] I. Majchrzak-Kucęba, et al., Treatment of flue gas in a CO2 capture pilot plant for a commercial CFB Boiler, Energies 14 (9) (2021) 2458.
[18] S.A. Rackley, 2 - Overview of carbon capture and storage, in: S.A. Rackley (Ed.), Carbon Capture and Storage (second Edition), Butterworth-Heinemann, Boston, 2017, pp. 23–36.
[19] E.S. Sanz-Pérez, et al., CO2 adsorption performance of amino-functionalized SBA-15 under post-combustion conditions, Int. J. Greenhouse Gas Control 17 (2013) 366–375.
[20] V.G. Gomes, K.W.K. Yee, Pressure swing adsorption for carbon dioxide sequestration from exhaust gases, Sep. Purif. Technol. 28 (2) (2002) 161–171.
[21] C.A. Grande, et al., Adsorption of Off-Gases from Steam Methane Reforming (H2, CO2, CH4, CO and N2) on Activated Carbon, Sep. Sci. Technol. 43 (6) (2008) 1338–1364.
[22] M. Ishibashi, et al., Technology for removing carbon dioxide from power plant flue gas by the physical adsorption method, Energ. Conver. Manage. 37 (6) (1996) 929–933.
[23] G. Li, et al., The role of water on postcombustion CO2 capture by vacuum swing adsorption: Bed layering and purge to feed ratio, AIChE J 60 (2) (2014) 673–689.
[24] J. Nastaj, B. Ambrożek, Analysis of gas dehydration in TSA system with multi-layered bed of solid adsorbents, Chem. Eng. Process. 96 (2015) 44–53.
[25] A. Qader, et al., Novel post-combustion capture technologies on a lignite fired power plant - results of the CO2CRC/H3 capture project, Energy Procedia 4 (2011) 1668–1675.
[26] Y.L. Fan, et al., High adsorption capacity and selectivity of SO2 over CO2 in a metal-organic framework, Inorg. Chem. 60 (1) (2021) 4–8.
[27] K. Tan, et al., Competitive Coadsorption of CO2 with H2O, NH3, SO2, NO, NO2, N2, O2, and CH4 in M-MOF-74 (M = Mg Co, Ni): The Role of Hydrogen Bonding, Chem. Mater. 27 (6) (2015) 2203–2217.
[28] H. Wang, et al., Experimental and numerical study of SO2 removal from a CO2/SO2 gas mixture in a Cu-BTC metal organic framework, J. Mol. Graph. Model. 96 (2020) 107533.
[29] M.S. AlQahtani, X. Wang, C. Song, Regenerable solid molecular basket sorbents for selective SO2 capture from CO2-rich gas streams, Catal. Today 371 (2021) 231–239.
[30] M. Berger, et al., Desulfurization process: understanding of the behaviour of the CuO/SBA-15 type SOx adsorbent in the presence of NO/NO2 and CO/CO2 flue gas environmental pollutants, Chem. Eng. J. 384 (2020) 123318.
[31] I. Matito-Martos, et al., Zeolite screening for the separation of gas mixtures containing SO2, CO2 and CO, PCCP 16 (37) (2014) 19884–19893.
[32] H. Yi, et al., Adsorption equilibrium and kinetics for SO2, NO, CO2 on zeolites FAU and LTA, J. Hazard. Mater. 203–204 (2012) 111–117.
[33] A. Czyżewski, et al., On competitive uptake of SO2 and CO2 from air by porous carbon containing CaO and MgO, Chem. Eng. J. 226 (2013) 348–356.
[34] Y. Guo, et al., Understanding the deactivation of K2CO3/AC for low-concentration CO2 removal in the presence of trace SO2 and NO2, Chem. Eng. J. 301 (2016) 325–333.
[35] J.H. Jacobs, et al., Removal of sulfur compounds from industrial emission using activated carbon derived from petroleum coke, Ind. Eng. Chem. Res. 58 (40) (2019) 18896–18900.
[36] Z. Aksu, F. Gönen, Binary biosorption of phenol and chromium(VI) onto immobilized activated sludge in a packed bed: Prediction of kinetic parameters and breakthrough curves, Sep. Purif. Technol. 49 (3) (2006) 205–216.
[37] M. Bastos-Neto, D.C.S. de Azevedo, S.M.P. de Lucena, Adsorption, in Kirk-Othmer Encyclopedia of, Chem. Technol. (2020) 1–59.
[38] D.M. Ruthven, Adsorption, fundamentals, in Kirk-Othmer encyclopedia of, Chem. Technol. (2001).
[39] F.J. Gutiérrez Ortiz, M. Barragán Rodríguez, R.T. Yang, Modeling of fixed-bed columns for gas physical adsorption, Chem. Eng. J. 378 (2019) 121985.
[40] M.S. Shafeeyan, W.M.A. Wan Daud, A. Shamiri, A review of mathematical modeling of fixed-bed columns for carbon dioxide adsorption, Chem. Eng. Res. Des. 92 (5) (2014) 961–988.
[41] F. Rouquerol, et al., Adsorption by powders and porous solids : principles, methodology and applications. Second edition. ed. 2014, Amsterdam: Elsevier/AP. xix, 626 pages.
[42] F. Dreisbach, R. Seif, H.W. Lösch, Adsorption equilibria of CO/H2 with a magnetic suspension balance: Purely gravimetric measurement, J. Therm. Anal. Calorim. 71 (1) (2003) 73–82.
[43] K. Lorenz, M. Wessling, How to determine the correct sample volume by gravimetric sorption measurements, Adsorption 19 (6) (2013) 1117–1125.
[44] M. Bastos-Neto, et al., Effects of textural and surface characteristics of microporous activated carbons on the methane adsorption capacity at high pressures, Appl. Surf. Sci. 253 (13) (2007) 5721–5725.
[45] M. Bastos-Neto, et al., Methane adsorption storage using microporous carbons obtained from coconut shells, Adsorption 11 (2005) 911–915.
[46] P.A.S. Moura, et al., Adsorption equilibria of CO2 and CH4 in cation-exchanged zeolites 13X, Adsorption 22 (1) (2016) 71–80.
[47] R.M. Siqueira, et al., Simple procedure to estimate mass transfer coefficients from uptake curves on activated carbons, Chem. Eng. Technol. 41 (8) (2018) 1622–1630.
[48] E. Vilarrasa-García, et al., CO2/CH4 adsorption separation process using pore expanded mesoporous silicas functionalizated by APTES grafting, Adsorption 21 (8) (2015) 565–575.
[49] R.B. Rios, et al., Evaluation of carbon dioxide–nitrogen separation through fixed bed measurements and simulations, Adsorption 20 (8) (2014) 945–957.
[50] R. Morales-Ospino, et al., Assessment of CO2 desorption from 13X zeolite for a prospective TSA process, Adsorption 26 (5) (2020) 813–824.
[51] R.G. Santiago, et al., Evaluation of the thermal regeneration of an amine-grafted mesoporous silica used for CO2/N2 separation, Adsorption 26 (2) (2020) 203–215.
[52] N.S. Wilkins, A. Rajendran, S. Farooq, Dynamic column breakthrough experiments for measurement of adsorption equilibrium and kinetics, Adsorption 27 (3) (2021) 397–422.
[53] H. Patel, Fixed-bed column adsorption study: a comprehensive review, Appl Water Sci 9 (3) (2019) 45.
[54] C. Tien, Chapter 6 - Fixed-Bed Adsorption Models and Fixed-Bed Design Calculations, in Introduction to Adsorption, C. Tien, Editor. 2019, Elsevier. p. 155-199.
[55] Unuabonah, E.I., M.O. Omorogie, and N.A. Oladoja, *5 - Modeling in Adsorption: Fundamentals and Applications*, in *Composite Nanoadsorbents*, G.Z. Kyzas and A.C. Mitropoulos, Editors. 2019, Elsevier. p. 85-118.
[56] M. Bastos-Neto, et al., Dynamic bed measurements of CO adsorption on microporous adsorbents at high pressures for hydrogen purification processes, Sep. Purif. Technol. 77 (2) (2011) 251–260.
[57] J. Tian, et al., CO2 capture by vacuum pressure swing adsorption from dry flue gas with a structured composite adsorption medium, J. Environ. Chem. Eng. 9 (5) (2021) 106037.
[58] T. Asadi, et al., CO2/CH4 Separation by Adsorption using Nanoporous Metal organic Framework Copper-Benzene-1,3,5-tricarboxylate Tablet, Chem. Eng. Technol. 36 (7) (2013) 1231–1239.
[59] F.A. Da Silva, J.A. Silva, A.E. Rodrigues, A general package for the simulation of cyclic adsorption processes, Adsorption 5 (3) (1999) 229–244.
[60] V.F.D. Martins, et al., Modeling of a cyclic sorption–desorption unit for continuous high temperature CO2 capture from flue gas, Chem. Eng. J. 434 (2022) 134704.
[61] R.B. Bird, W.E. Stewart, E.N. Lightfoot, Transport phenomena, 2nd rev. ed., John Wiley & Sons, New York; Chichester, 2007.
[62] N. Casas, et al., Fixed bed adsorption of CO2/H2 mixtures on activated carbon: experiments and modeling, Adsorption 18 (2) (2012) 143–161.
[63] D.D. Do, *Adsorption analysis : equilibria and kinetics*. Series on chemical engineering, Imperial College Press. xxi, London, 1998, p. 892 p..
[64] B.E. Poling, J.M. Prausnitz, J.P. O'Connell, The properties of gases and liquids, 5th ed., McGraw-Hill, New York, 2001.
[65] M.F. Edwards, J.F. Richardson, Gas dispersion in packed beds, Chem. Eng. Sci. 23 (2) (1968) 109–123.
[66] W. Kay, Gases and vapors at high temperature and pressure - density of hydrocarbon, Ind. Eng. Chem. 28 (9) (1936) 1014–1019.
[67] D.M. Ruthven, Principles of adsorption and adsorption processes, Wiley. xxiv, New York, 1984, p. 433 p..
[68] A.G. Dixon, D.L. Cresswell, Theoretical prediction of effective heat transfer parameters in packed beds, AIChE J 25 (4) (1979) 663–676.
[69] T.L. Bergman, et al., Fundamentals of heat and mass transfer. 8th ed. 2019, Hoboken, NJ: Wiley. 992 p.
[70] R.H. Perry, D.W. Green, Perry's chemical engineers' handbook, 8th ed., McGraw-Hill, New York, 2008.
[71] M.H. Ketko, G. Kamath, J.J. Potoff, Development of an Optimized Intermolecular Potential for Sulfur Dioxide, J. Phys. Chem. B 115 (17) (2011) 4949–4954.
[72] J.J. Potoff, J.I. Siepmann, Vapor–liquid equilibria of mixtures containing alkanes, carbon dioxide, and nitrogen, AIChE J 47 (7) (2001) 1676–1682.
[73] G.C. Maitland, et al., Intermolecular Forces – Their Origin and Determination, Clarendon Press, Oxford, 1981, p. 616.
[74] D.V. Gonçalves, et al., Prediction of the monocomponent adsorption of H2S and mixtures with CO2 and CH4 on activated carbons, Colloids Surf A Physicochem Eng Asp 559 (2018) 342–350.
[75] A.P. Guimarães, et al., Diffusion of linear paraffins in silicalite studied by the ZLC method in the presence of CO2, Adsorption 16 (1) (2010) 29–36.
[76] J.C.A. de Oliveira, et al., On the influence of heterogeneity of graphene sheets in the determination of the pore size distribution of activated carbons, Adsorption 17 (5) (2011) 845–851.

[77] S.M.P. Lucena, et al., Fingerprints of heterogeneities from carbon oxidative process: A reactive molecular dynamics study, Microporous Mesoporous Mater. 304 (2020) 109061.
[78] S.M.P. Lucena, et al., Pore size analysis of carbons with heterogeneous kernels from reactive molecular dynamics model and quenched solid density functional theory, Carbon 183 (2021) 672–684.
[79] J.C.A. de Oliveira, et al., Representative pores: an efficient method to characterize activated carbons, Front. Chem. 8 (2021) 1–9.
[80] R.L.C.B. Menezes, et al., Insights on the Mechanisms of H2S Retention at Low Concentration on Impregnated Carbons, Ind. Eng. Chem. Res. 57 (6) (2018) 2248–2257.
[81] W.A. Steele, The physical interaction of gases with crystalline solids: I. Gas-solid energies and properties of isolated adsorbed atoms, Surf. Sci. 36 (1) (1973) 317–352.
[82] R. Krishna, J.M. van Baten, Elucidation of selectivity reversals for binary mixture adsorption in microporous adsorbents, ACS Omega 5 (15) (2020) 9031–9040.
[83] R. Anderson, D.A. Gómez-Gualdrón, Deep learning combined with IAST to screen thermodynamically feasible MOFs for adsorption-based separation of multiple binary mixtures, J. Chem. Phys. 154 (23) (2021) 234102.
[84] F. Chen, et al., Deep Desulfurization with Record SO2 Adsorption on the Metal-Organic Frameworks, J. Am. Chem. Soc. 143 (24) (2021) 9040–9047.
[85] J. Chen, L.S. Loo, K. Wang, An Ideal Absorbed Solution Theory (IAST) study of adsorption equilibria of binary mixtures of methane and ethane on a templated carbon, J. Chem. Eng. Data 56 (4) (2011) 1209–1212.
[86] M. Rahimi, J.K. Singh, F. Müller-Plathe, Adsorption and separation of binary and ternary mixtures of SO2, CO2 and N2 by ordered carbon nanotube arrays: grand-canonical Monte Carlo simulations, PCCP 18 (5) (2016) 4112–4120.
[87] K.S. Walton, D.S. Sholl, Predicting multicomponent adsorption: 50 years of the ideal adsorbed solution theory, AIChE J 61 (9) (2015) 2757–2762.
[88] J.L.B. de Oliveira, et al., Effect of ultramicropores on the mechanisms of H2S retention from biogas, Chem. Eng. Res. Des. 154 (2020) 241–249.
[89] X. Zhou, et al., Thermodynamics for the adsorption of SO2, NO and CO2 from flue gas on activated carbon fiber, Chem. Eng. J. 200–202 (2012) 399–404.
[90] H. Yi, et al., Adsorption of SO2, NO, and CO2 on Activated Carbons: Equilibrium and Thermodynamics, J. Chem. Eng. Data 59 (5) (2014) 1556–1563.
[91] X. Dong, et al., Investigation of Competitive Adsorption Properties of CO/CO2/O2 onto the Kailuan Coals by Molecular Simulation, ACS Omega 7 (23) (2022) 19305–19318.
[92] A.K. Mohammad, N.S. Sabeeh, Comparative study for adsorption of hydrogen-methane mixtures on activated carbon and 5a molecular sieve, Braz. J. Chem. Eng. 35 (2018).
[93] R.B. Rios, et al., Studies on the Adsorption Behavior of Co2-Ch4 Mixtures Using Activated Carbon, Braz. J. Chem. Eng. 30 (4) (2013) 939–951.
[94] H. Deng, et al., Adsorption equilibrium for sulfur dioxide, nitric oxide, carbon dioxide, nitrogen on 13X and 5A zeolites, Chem. Eng. J. 188 (2012) 77–85.
[95] Z. Li, et al., Capture of H2S and SO2 from trace sulfur containing gas mixture by functionalized UiO-66(Zr) materials: A molecular simulation study, Fluid Phase Equilib. 427 (2016) 259–267.
[96] E. Atanes, et al., Adsorption of SO2 onto waste cork powder-derived activated carbons, Chem. Eng. J. 211–212 (2012) 60–67.
[97] S. Sircar, et al., Isosteric Heat of Adsorption: Theory and Experiment, J. Phys. Chem. B 103 (31) (1999) 6539–6546.
[98] P.G. Gray, D.D. Do, Adsorption and desorption of gaseous sorbates on a bidispersed particle with Freundlich isotherm: III. Contribution of surface diffusion to the sorption dynamics of sulphur dioxide on activated carbon, Gas Sep. Purif. 4 (3) (1990) 149–157.
[99] A.C. Lua, T. Yang, Theoretical and experimental SO2 adsorption onto pistachio-nut-shell activated carbon for a fixed-bed column, Chem. Eng. J. 155 (1) (2009) 175–183.
[100] T.L.P. Dantas, et al., Carbon dioxide–nitrogen separation through adsorption on activated carbon in a fixed bed, Chem. Eng. J. 169 (1) (2011) 11–19.
[101] K.R. Dupre, et al., Investigation of computational upscaling of adsorption of SO2 and CO2 in fixed bed columns, Adsorption 25 (4) (2019) 773–782.
[102] L. Ding, A.Ö. Yazaydin, How well do metal-organic frameworks tolerate flue gas impurities? J. Phys. Chem. C 116 (43) (2012) 22987–22991.
[103] D.L. Montenegro, et al., Prediction of SO2 adsorption in activation carbon via molecular simulation. 2023: submitted to Microporous and Mesoporous Materials. p. 21. Unpublished work Available at: https://lab3d.ufc.br/wp-content/uploads/2023/10/Manuscript_SO2_CA_-Danielle.pdf; https://lab3d.ufc.br/wp-content/uploads/2023/10/SO2_support-information.pdf; Password: **lab3d**.

Glossary

BET: Brunauer-Emmett-Teller
C141-S: Activated carbon supplied by Indústrias Químicas Carbomafra S.A. (Brazil)
CaO: Calcium oxide
CO_2: Carbon dioxide
DR: Dubinin-Radushkevich
GC: Gas cromatograph
He: Helium
H_2O: Water
IAST: Ideal Adsorbed Solution Theory
IEA: International Energy Agency
LDF: Linear Driving Force
LJ: Lennard-Jones
MgO: Magnesium oxide
MOF: Metal-organic Framework
N_2: Nitrogen gas
NO_X: Oxides of nitrogen
NVT: Canonical ensemble: number of particles in the system (N), system's volume (V), and the absolute temperature (T).
O_2: Oxygen gas
OCFEM: Orthogonal collocation on finite elements
P/P_0: Relative pressure (equilibrium pressure divided by saturation pressure)
ppmv: Parts per million (10^6) by volume
PVSA: Pressure/Vacuum Swing Adsorption
rMD: Reactive Molecular Dynamics
SBA-15: Santa Barbara Amorphous-15 (mesoporous silica sieve)
SO_2: Sulfur dioxide
TraPPE: Transferable Potentials for Phase Equilibria Force Field